Research Square

Preprints are preliminary reports that have not undergone peer review.
They should not be considered conclusive, used to inform clinical practice,
or referenced by the media as validated information.

Hierarchically Porous $ZnTiO_3$/Zeolite Composites with Optimised

RAM KUMAR POOMANI

prrchem@tce.edu

Thiagarajar College of Engineering

Nichelson A

Kalaignarkarunanidhi Institute of Technology

Mothi Paul E

PSN College of Engineering and Technologyin

Alwin S

The American College

Karthickprabhu S

Thiagarajar College of Engineering, Madurai

Tamilarasan K

Alagappa University

Research Article

Keywords: ZnTiO3/zeolite composite, Supercapattery, Hierarchical porous electrode, Charge-storage kinetics, Electrochemical energy storage, Battery-type electrode.

Posted Date: October 30th, 2026

DOI: https://doi.org/10.21203/rs.3.rs-10902419/v1

License: This work is licensed under a Creative Commons Attribution 4.0 International License.
Read Full License

Additional Declarations: No competing interests reported.

Hierarchically Porous $ZnTiO_3$/Zeolite Composites with Optimised Charge-Storage Kinetics for Alkaline Supercapattery Applications

P. Ram Kumar[*], A. Nichelson[b], E. Mothi Paul[c], S. Alwin[d], S. Karthickprabhu[e],

[a]*Advanced Materials Lab-Centre of Excellence in Hydrogen Energy Research, Department of Chemistry, Thiagarajar College of Engineering, Madurai-625 015, Tamil Nadu, India.*
[b]*Department of Physics, Kalaignarkarunanidhi Institute of Technology, Coimbatore, 641402, Tamil Nadu, India.*
[c]*Department of Chemistry, School of Basic Engineering and Sciences, PSN College of Engineering and Technology, Melathediyoor, Tirunelveli 627 152, Tamil Nadu, India.*
[d]*Department of Chemistry, The American College, Madurai-625 002, Tamil Nadu, India.*
[e]*Centre of Excellence in Materials Research and Energy Solutions, Department of Physics, Thiagarajar College of Engineering, Madurai-625 015, Tamil Nadu, India.*
[f]*Advanced Materials and Thin Film Lab, Department of Physics, Alagappa University, Karaikudi-630003, India.*

Corresponding author E-mail: dr.ramchem93@gmail.com

Abstract

$ZnTiO_3$/zeolite composites with varying zeolite loadings were synthesised through a solution-assisted mixing method and investigated as electrode materials for alkaline supercapattery applications. Structural characterisation confirmed the coexistence of crystalline $ZnTiO_3$, Zn_2TiO_4, and zeolite without altering the crystal structure or chemical states of the constituent phases. Incorporating zeolite improved particle dispersion and created a porous architecture that facilitated electrolyte accessibility and ion transport. Electrochemical investigations in 3 M KOH revealed battery-type Faradaic charge-storage behaviour dominated by diffusion-controlled Faradaic reactions with an increased surface-controlled contribution after zeolite incorporation. Among the investigated compositions, the ZT-20 electrode exhibited the optimum electrochemical performance, delivering a specific capacity of 149 C g^{-1} (41.39 mAh g^{-1}) at 1 A g^{-1}, a low charge-transfer resistance of 8.92 Ω, and approximately 70% capacity retention after 5000 charge–discharge cycles. The enhanced performance is attributed to the synergistic effect of the porous zeolite framework and electrochemically active $ZnTiO_3$, which promotes efficient electrolyte diffusion, rapid charge transfer, and improved active-site utilisation. These findings demonstrate that $ZnTiO_3$/zeolite composites are promising, low-cost electrode materials for high-performance alkaline supercapattery energy storage applications.

Keywords: $ZnTiO_3$/zeolite composite; Supercapattery; Hierarchical porous electrode; Charge-storage kinetics; Electrochemical energy storage; Battery-type electrode.

1. Introduction

The pressing global issues of environmental pollution, climate change, and energy scarcity have spurred the quest to develop innovative materials and technologies [1–4]. Sustainable energy conversion and storage solutions have become essential amid escalating energy demands driven by rapid societal growth and the significant consumption of fossil fuels. The development of renewable energy technologies was catalysed to mitigate environmental issues associated with fossil fuels [5–8]. Additionally, components derived from renewable bioresources have garnered significant interest for their potential to provide affordable, sustainable clean energy [9–11]. However, renewable energy generation is intermittent, creating an imbalance between generation and storage. Hence, to ensure a sustainable energy supply, renewable energy technology entails energy storage devices. Supercapacitors, known for their rapid charge-discharge capabilities, have emerged as a promising alternative to traditional batteries for energy storage. Supercapacitors outperform batteries because they deliver high power density, long cycle life, and enhanced safety features [12–16]. Supercapacitors are the ideal option for applications that demand rapid energy delivery, including automotive, consumer electronics, aerospace, and renewable energy sectors [17]. The performance of supercapacitors is influenced mainly by the choice of materials utilized in fabricating their electrodes [18,19]. Generally, electric double-layer capacitors (EDLCs) rely on the accumulation of electrostatic charge at the interface and employ activated carbon, CNTs, graphene, and other carbon nanostructures as electrode materials. On the other hand, pseudo-capacitors leverage faradaic reactions with materials such as metal oxides and conducting polymers to achieve greater capacitance [20,21]. However, carbon-based materials excel in cycling stability but tend to have limited capacitance, whereas metal oxides achieve high capacitance but suffer from low electrical conductivity and poor

cycling stability at high current densities. Thus, there has been a considerable surge in the development of cutting-edge electrode materials like aerogels, metal organic frameworks (MOF), covalent organic frameworks (COFs), MXenes, and metal nitrides that aim to increase capacitance, electrical conductivity, and cycle stability, ultimately focusing on enhancing the energy and power densities of supercapacitors [13,22].

Composite electrode materials achieve synergistic effects by combining components in a balanced manner, overcoming the drawbacks of each. A pertinent example is the integration of carbon nanotubes (CNT) or graphene within activated carbon composites, which results in a synergistic effect. The robust activated carbon imparts stability, while the nanoparticles increase the specific surface area and porosity, ultimately enhancing both capacity and high-rate performance [23]. Most studies have focused on combinations such as metal oxides with conductive polymers or carbon-based materials for their potential use in supercapacitor applications [7,18]. Among metal oxides, zinc titanate ($ZnTiO_3$) has attracted considerable interest for its appealing balance of electrochemical stability and electrical conductivity. Recently, $ZnTiO_3$ is employed as a photocatalyst for the degradation of p-nitrophenol and as a photoanode material in quasi-solid de-sensitised solar cells. It is observed that the recombination reactions are suppressed due to better electronic conductivity [24–27]. Furthermore, $ZnTiO_3$ has demonstrated a commendable charge storage capacity when utilised as an electrode material in supercapacitors, attributed to its adjustable morphology [28]. Despite its promising properties, zinc titanate suffers from certain limitations, including a lower specific surface area, porosity, and a tendency to agglomerate, which hinder its practical use in supercapacitors.

Recent advances in electrochemical energy storage have established zinc titanate ($ZnTiO_3$) as a promising battery-type electrode material owing to its chemical stability, environmental

compatibility, multiple redox-active sites, and favorable ionic transport characteristics. Nevertheless, the practical electrochemical performance of pristine $ZnTiO_3$ remains constrained by its relatively low electrical conductivity, particle agglomeration, and sluggish ion diffusion during repeated charge–discharge processes. Consequently, recent research has focused on morphology engineering and composite design to overcome these limitations. Hydrothermally synthesised $ZnTiO_3$ nanoflakes have demonstrated enhanced electrochemical performance through hierarchical architectures that promote electrolyte penetration and ion transport, delivering a specific capacitance of 132 F g^{-1} in a symmetric configuration and 240 F g^{-1} in an asymmetric $ZnTiO_3$//activated carbon device, together with an energy density of 27 Wh kg^{-1} and excellent cycling durability, confirming the potential of $ZnTiO_3$ for practical supercapacitor applications [28]. More recently, $ZnTiO_3$/carbon nanofiber composites have achieved a high specific capacity of 199 mAh g^{-1} with outstanding long-term cycling stability, demonstrating that conductive scaffolds effectively accelerate electron transport and improve active-site utilization [29]. Likewise, sol–gel-derived $ZnTiO_3$ nanostructures have exhibited a high specific capacitance of 557 F g^{-1}, while titanate-based materials such as $CaZnTi_2O_4$ and $ZnCe_{0.3}Ti_{0.7}O_3$ have further expanded the applicability of zinc titanates toward multifunctional energy-storage and sensing platforms [30,31]. These studies collectively demonstrate that the electrochemical performance of zinc titanates is governed not only by their intrinsic Faradaic activity but also by electrode architecture, electrolyte accessibility, and interfacial charge-transfer kinetics. Despite these significant advances, the integration of $ZnTiO_3$ with porous aluminosilicate frameworks has received little attention, particularly for supercapattery applications.

Zeolites are a class of porous aluminosilicate minerals known for their high surface area, tunable porosity, and ion-exchange capabilities, which are used in applications such as catalysis, gas

separation, and water purification [32]. Zeolites are employed as templates to tailor electrode materials with desired porosity and particle size for supercapacitors. Zeolite-templated carbon possesses an ordered hierarchical porous structure with a very high surface area and has recently garnered attention as a promising material for electrochemical energy storage due to its extensive microporous structure [33,34]. These micropores provide ample active sites for electrolyte, enhancing ion mobility. Recently, it was reported that combining microporous MOFs with zinc titanate retards the recombination reactions in dye-sensitised solar cells, thus increasing the open-circuit voltage [26]. Similarly, incorporating zeolites with metal oxides has shown significant promise, as the composite combines the benefits of both components. SnO_2 quantum dot-dispersed zeolitic imidazolate framework as electrode material showed a specific capacitance of 931 F/g [35]. An iron oxide complexed with a nickel-based zeolite, used as an electrode material, exhibited a high specific capacitance of 739.8 F/g at a current density of 1 A [36]. Cobalt-loaded zeolite exhibits a high specific capacitance of 550 F/g at 1 A due to its high porosity, which facilitates electrolyte penetration into the pores and provides access to the electrode surface [37]. Previous studies have demonstrated that zeolite-based composite electrodes exhibit predominant battery-type/pseudocapacitive charge-storage behaviour with enhanced energy-storage capability, owing to their porous framework and efficient ion-transport pathways [33,36]. Therefore, coupling zeolite with $ZnTiO_3$ is expected to retain the intrinsic battery-type Faradaic behaviour of $ZnTiO_3$ while improving electrolyte accessibility, active-site utilisation, and charge-transfer kinetics, thereby enhancing the overall electrochemical performance of $ZnTiO_3$/zeolite composite electrodes.

The present work focuses on the synthesis and electrochemical performance of a $ZnTiO_3$-Zeolite composite as a supercapacitor electrode material. Zeolite provides hierarchical porosity and high

surface area while $ZnTiO_3$ offers enhanced pseudocapacitive behavior. The synergy between these two materials is expected to enhance electrochemical performance by enabling rapid ion diffusion and reducing internal resistance, thereby improving conductivity and cycling stability. Zeolite can also mitigate agglomeration of $ZnTiO_3$ particles, thereby creating a more uniform electrode structure that improves both capacitance and durability. Thus, a $ZnTiO_3$-zeolite composite represents a novel and potentially practical approach to addressing the common limitations faced by traditional supercapacitor materials. The research investigates how the synergistic combination of $ZnTiO_3$ and zeolite influences capacitance and cycle stability.

2. Experimental

2.1 Materials

Commercial synthetic zeolite (aluminosilicate, CAS No. 1318-02-1, Product No. 96096) was purchased from Sigma-Aldrich and used as the porous support material. Zinc acetate dihydrate ($Zn(CH_3COO)_2 \cdot 2H_2O$, Loba Chemie, India) and titanium(IV) isopropoxide (TTIP, 97%, Sigma-Aldrich) were employed as zinc and titanium precursors, respectively. Methanol, acetic acid, N-methyl-2-pyrrolidone (NMP), poly(vinylidene fluoride) (PVDF), and conductive carbon black (Super P) were of analytical grade and used without further purification. Deionised water (18.2 MΩ cm) obtained from a Millipore purification system was used throughout the experiments.

2.2 Synthesis of $ZnTiO_3$

pristine $ZnTiO_3$ (ZT) was synthesised by a solid-state reaction method. Zinc acetate dihydrate and titanium(IV) isopropoxide were mixed in a stoichiometric Zn: Ti molar ratio of 1:1 using acetic acid as the dispersion medium. The homogeneous precursor mixture was dried and subsequently calcined in air at 900 °C for 10 h to obtain crystalline zinc titanate powder.

2.3 Preparation of $ZnTiO_3$/Zeolite Composites

$ZnTiO_3$/zeolite composites were prepared by a solution-assisted mixing method. Initially, the required amount of $ZnTiO_3$ powder was dispersed in 100 mL of methanol under magnetic stirring for 30 min followed by ultrasonication for an additional 30 min. Predetermined quantities of commercial zeolite were then gradually introduced into the suspension under continuous stirring to ensure homogeneous mixing. The resulting suspension was further ultrasonicated for 30 min and allowed to settle. The precipitate was collected by decantation and dried in a vacuum oven at 50 °C for 3 h. Composites with varying zeolite contents were prepared, maintaining a total mass of 1 g. The compositions were designated as ZT-10, ZT-20, ZT-30, and ZT-40, corresponding to 10, 20, 30, and 40 wt% zeolite, respectively. The synthesised powders were stored in airtight containers prior to characterisation and electrochemical evaluation. A schematic representation of the synthesis procedure is shown in Fig. 1.

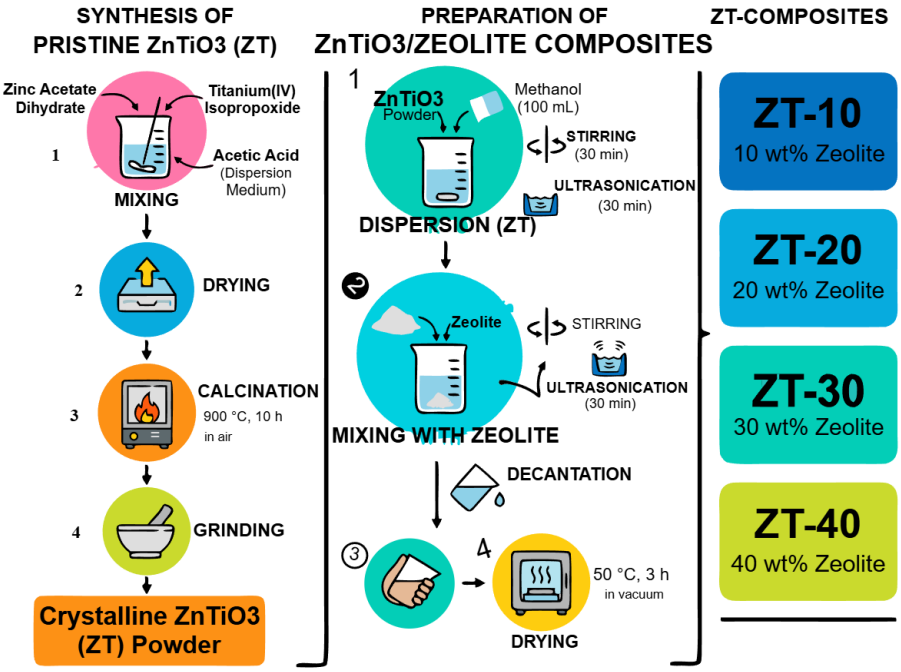


Fig. 1. Schematic representation of the synthesis of pristine $ZnTiO_3$ and the preparation of $ZnTiO_3$/zeolite composites with different zeolite loadings (10–40 wt%).

2.4 Characterization Techniques

The crystal structures of the synthesised materials were examined by powder X-ray diffraction (PXRD) using a Bruker D8 Advance ECO diffractometer equipped with Cu Kα radiation (λ = 1.5406 Å) over a 2θ range of 20–80°. Fourier-transform infrared (FTIR) spectra were recorded in the range of 400–4000 cm^{-1} to identify the characteristic functional groups and metal–oxygen vibrations. Surface morphology and elemental composition were investigated using a Carl Zeiss EVO18 field-emission scanning electron microscope (FESEM) equipped with an energy-dispersive X-ray spectroscopy (EDS) detector. X-ray photoelectron spectroscopy (XPS) measurements were performed using a SPECS GmbH spectrometer with Mg Kα radiation and a Phoibos 100-MCD hemispherical analyser operating under ultra-high vacuum conditions. Binding energies were calibrated using the C 1s peak at 284.8 eV.

2.5 Electrode Fabrication and Electrochemical Measurements

Electrochemical measurements were carried out using a conventional three-electrode configuration in 3 M KOH aqueous electrolyte. Nickel foam (1 × 1 cm^2) served as the current collector and was sequentially cleaned with hydrochloric acid, deionised water, ethanol, and acetone, then dried at 60 °C. The working electrode slurry consisted of 80 wt% active material, 10 wt% Super P conductive carbon, and 10 wt% PVDF binder dispersed in NMP to obtain a homogeneous paste. The slurry was uniformly coated onto the pretreated nickel foam and dried at 80 °C overnight. The average mass loading of the active material was maintained at 3.2 mg cm^{-2}. Electrochemical measurements were performed using the composite-coated nickel foam as the working electrode, a platinum wire as the counter electrode, and a saturated calomel electrode (SCE) as the reference electrode. Cyclic voltammetry (CV) measurements were carried out within the selected potential window at scan rates of 5-100 mV s^{-1} to investigate the charge-

storage mechanism and rate capability of the electrodes. Galvanostatic charge–discharge (GCD) measurements were performed at current densities of 1-5 A g^{-1} to evaluate specific capacity and rate performance. Electrochemical impedance spectroscopy (EIS) measurements were recorded over the frequency range of 100 kHz to 0.01 Hz using an AC perturbation amplitude of 5 mV. Long-term cycling stability was evaluated by repeated GCD measurements for 5000 consecutive charge–discharge cycles at a current density of 5 A g^{-1}. All electrochemical measurements were performed at room temperature. Unless otherwise stated, no iR compensation was applied during electrochemical measurements.

2.6 Dunn's Kinetic Analysis

The charge-storage mechanism of the prepared electrodes was quantitatively analysed using Dunn's method based on cyclic voltammetry (CV) data acquired at scan rates of 1-100 mV s^{-1}. The experimental current response at each potential was separated into surface-controlled (capacitive) and diffusion-controlled contributions according to:

$$i(V) = k_1 v + k_2 v^{1/2} \quad (1)$$

where $i(V)$ is the measured current at a given potential, v is the scan rate, $k_1 v$ represents the surface-controlled current contribution, and $k_2 v^{1/2}$ corresponds to the diffusion-controlled current contribution.

For each electrode, the raw CV datasets obtained at different scan rates were imported into Python (Python 3.x) for numerical analysis. The forward and reverse scans were identified from the experimental potential profile, and the current values at each scan rate were aligned onto a common potential grid using linear interpolation only when required. At every potential, the current was transformed according to:

$$\frac{i(V)}{v^{1/2}} = k_1 v^{1/2} + k_2 \quad (2)$$

The coefficients k_1 and k_2 were determined by ordinary least-squares linear regression using all available scan rates. The regression quality was evaluated using the coefficient of determination (R^2), standard error, and residual analysis.

The surface-controlled and diffusion-controlled currents were reconstructed using the calculated kinetic coefficients according to:

$$i_{\text{cap}} = k_1 v \quad (3)$$

$$i_{\text{diff}} = k_2 v^{1/2} \quad (4)$$

The reconstructed current was subsequently obtained as:

$$i_{\text{rec}} = i_{\text{cap}} + i_{\text{diff}} \quad (5)$$

The accuracy of the reconstruction was assessed by comparing the reconstructed current with the experimental CV response using the root-mean-square error (RMSE), mean absolute error (MAE), and maximum deviation. The quantitative contributions of the surface-controlled and diffusion-controlled processes were determined by numerically integrating the reconstructed current over the entire potential window using the trapezoidal rule. The capacitive and diffusion-controlled contributions were expressed as percentages of the total integrated current at each scan rate. The obtained kinetic parameters were used to construct potential-dependent k_1 and k_2 profiles, reconstructed CV curves, and scan-rate-dependent capacitive contribution plots.

3. Results and Discussion

3.1. X-ray Diffraction Analysis

Fig.2 shows the PXRD patterns of pristine $ZnTiO_3$ (ZT) and $ZnTiO_3$/zeolite composites containing different zeolite loadings. The diffraction pattern of the pristine sample confirms the formation of crystalline zinc titanate after calcination at 900 °C. The major reflections at 2θ = 31.8°, 35.7°, 38.8°, 41.0°, and 47.2° are indexed to the (104), (110), (113), (400), and (204) planes of hexagonal $ZnTiO_3$ (ICDD PDF No. 14-0033). Additional reflections located at 52.8°,

56.3°, 61.7°, 62.6°, 68.9°, and 69.5° correspond to the (220), (311), (511), (214), (440), and (620) planes of cubic Zn_2TiO_4 (ICDD PDF No. 02-1033), indicating the coexistence of both zinc titanate phases. Such mixed-phase formation is commonly observed in ZnO–TiO_2 systems calcined at temperatures around 900 °C due to the phase evolution of zinc titanates during solid-state reactions [26,27,38]. Weak reflections near 27°, 29°, and 54° are assigned to trace rutile and brookite TiO_2, suggesting the presence of a small amount of unreacted or transformed titania. Their relatively low intensity indicates that these phases are minor and do not significantly affect the overall crystal structure of the zinc titanate matrix.

Following zeolite incorporation, the characteristic diffraction peaks of $ZnTiO_3$ and Zn_2TiO_4 remain unchanged, demonstrating that the solution-assisted mixing process preserves the crystal structure of zinc titanate without generating additional crystalline reaction products. The composite containing 40 wt% zeolite (ZT-40) exhibits weak diffraction features in the low-angle region (10–25°), characteristic of the aluminosilicate zeolite framework, confirming the successful incorporation of the porous zeolite phase. A slight broadening of the zinc titanate reflections is observed with increasing zeolite content. Since the composites were prepared by physical mixing rather than high-temperature co-calcination, this broadening is more reasonably attributed to the increasing contribution of the less crystalline zeolite phase and reduced diffraction coherence within the composite rather than to a structural transformation of $ZnTiO_3$. Overall, the PXRD results confirm the coexistence of crystalline $ZnTiO_3$, Zn_2TiO_4, and zeolite while demonstrating that the composite preparation route preserves the crystal structures of the individual components.

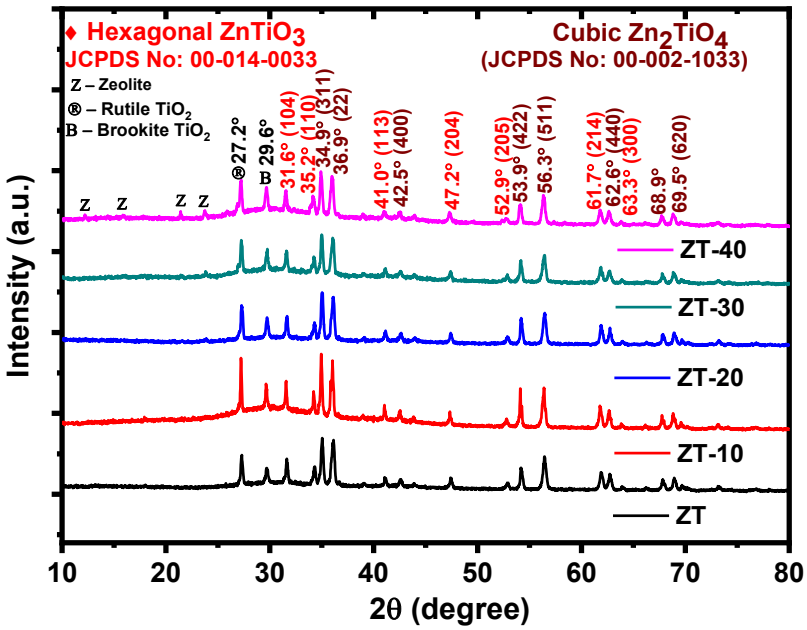


Fig. 2. Powder X-ray diffraction (PXRD) patterns of pristine $ZnTiO_3$ (ZT) and zinc titanate/zeolite (ZTZ) composites containing different zeolite loadings.

3.2. FTIR Analysis

Fig.3 presents the FTIR spectra of pristine $ZnTiO_3$ (ZT) and $ZnTiO_3$/zeolite composites with different zeolite loadings. The spectra confirm the coexistence of zinc titanate and the aluminosilicate framework while indicating that the characteristic vibrational features of both components are retained after composite formation. The FTIR spectrum of pristine ZT exhibits characteristic absorption bands in the 400–700 cm^{-1} region, corresponding to lattice vibrations of Zn–O, Ti–O, and Zn–O–Ti linkages within the zinc titanate structure. The bands observed at approximately 436, 501, 600, and 667 cm^{-1} agree well with the reported vibrational modes of crystalline zinc titanate and confirm the formation of the oxide framework [39–41]. Following zeolite incorporation, a prominent absorption band appears at approximately 1003–1005 cm^{-1} for all composite samples (ZT-10 to ZT-40). This band is assigned to the asymmetric stretching vibration of T–O–T (T = Si or Al) linkages associated with the aluminosilicate framework and serves as a characteristic fingerprint of the zeolite phase. The intensity of this band increases progressively with increasing zeolite content, confirming the successful incorporation of zeolite into the $ZnTiO_3$ matrix while preserving its framework structure.

The low-wavenumber region also undergoes slight broadening after zeolite addition because the Zn–O/Ti–O lattice vibrations of zinc titanate overlap with the T–O bending vibrations of the aluminosilicate framework. The retention of the characteristic metal–oxygen vibrations, together with the emergence of the zeolite framework band, indicates that both constituents coexist without the formation of any new detectable infrared-active phases. A broad absorption centred at approximately 3420–3450 cm^{-1} together with a weaker band near 1635 cm^{-1} is observed for the zeolite-containing composites. These bands are attributed to O–H stretching and H–O–H bending vibrations of surface hydroxyl groups and adsorbed water, respectively. Their increased intensity with higher zeolite loading reflects the hydrophilic nature of the porous aluminosilicate framework. Overall, the FTIR results complement the PXRD analysis by confirming the successful incorporation of zeolite into the $ZnTiO_3$ matrix while preserving the characteristic structural features of both components. The coexistence of Zn–O/Ti–O lattice vibrations and aluminosilicate framework bands demonstrates that the composite preparation method maintains the structural integrity of the individual phases without introducing significant changes to their chemical bonding.

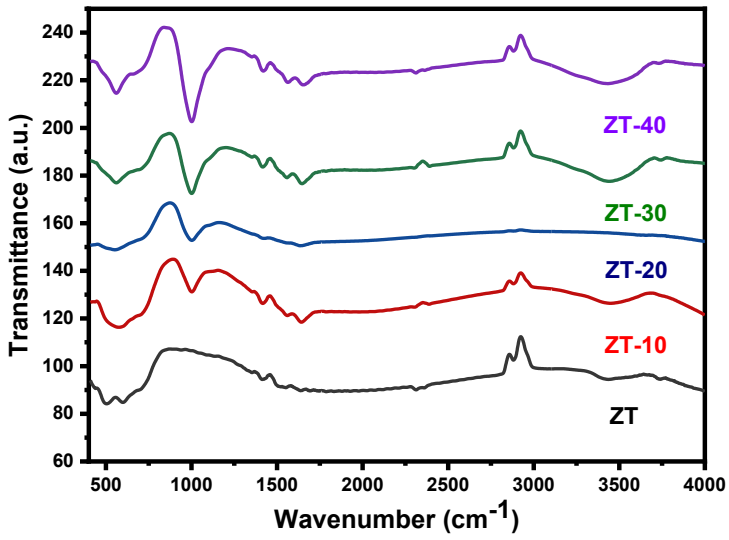


Fig. 3. FTIR spectra of pristine $ZnTiO_3$ (ZT) and zinc titanate/zeolite composites (ZTZ-10, ZTZ-20, ZTZ-30, and ZTZ-40) with varying zeolite contents, showing the characteristic metal–oxygen lattice vibrations and zeolitic aluminosilicate framework vibrations.

3.3. X-ray Photoelectron Spectroscopy Analysis

The surface chemical composition and oxidation states of the ZT-40 composite were investigated by XPS, and the corresponding survey and high-resolution spectra are presented in Fig. S1 and

Fig. 4. The survey spectrum confirms the presence of Zn, Ti, O, Si, Al, Na, and C, indicating the successful formation of the $ZnTiO_3$/zeolite composite with no detectable impurity elements. The Zn and Ti signals originate from the zinc titanate phase, whereas Si, Al, and Na are characteristic constituents of the aluminosilicate zeolite framework. The quantified surface elemental composition (Table 1) consists of O (41.42 at.%), C (31.67 at.%), Al (8.15 at.%), Si (7.80 at.%), Na (5.29 at.%), Zn (3.08 at.%), and Ti (2.58 at.%). The relatively higher concentrations of Si, Al, and Na compared with Zn and Ti indicate surface enrichment of the zeolite phase, which is expected considering the surface-sensitive nature of XPS (sampling depth 5–10 nm) and the intimate coverage of zinc titanate particles by the porous aluminosilicate matrix. The C 1s peak at 284.8 eV was used as the internal reference for charge correction [42].

The high-resolution Zn 2p spectrum (Fig. 4a) exhibits two well-resolved peaks centred at 1021.4 eV (Zn $2p_{3/2}$) and 1044.5 eV (Zn $2p_{1/2}$), with a spin-orbit splitting of approximately 23.1 eV. These binding energies agree well with the reported values for Zn^{2+} in zinc titanate and confirm that zinc exists predominantly in the divalent oxidation state coordinated with lattice oxygen [43]. No additional components or satellite features associated with metallic zinc or reduced zinc species are observed. The Ti 2p spectrum (Fig. 4b) consists of Ti $2p_{3/2}$ and Ti $2p_{1/2}$ peaks located at 458.7 and 464.4 eV, respectively, with a spin-orbit separation of approximately 5.7 eV. These values are characteristic of Ti^{4+} in the titanate lattice and indicate that titanium remains in its fully oxidized state after composite formation. The absence of lower binding-energy components suggests that no detectable Ti^{3+} species are present [44]. The deconvoluted O 1s spectrum (Fig. 4c) can be resolved into two components centred at approximately 532.2 and 531.4 eV. The dominant peak at 532.2 eV is assigned to lattice oxygen (O^{2-}) associated with Zn–O, Ti–O, and Si–O bonds within the $ZnTiO_3$ and aluminosilicate frameworks. The higher binding-energy component at 531.4 eV is attributed to surface hydroxyl groups (–OH) and adsorbed oxygen-containing species, including chemisorbed oxygen and molecularly adsorbed water, which are commonly present on metal oxide and porous zeolite surfaces. The relatively higher intensity of this component is consistent with the hydrophilic nature of the zeolite framework. Although defect-related oxygen species may contribute within this binding-energy region, XPS alone cannot unequivocally distinguish oxygen vacancies from hydroxylated surface species; therefore, the higher binding-energy peak is conservatively assigned to surface oxygen-containing species.

This interpretation is consistent with the broad O–H stretching and H–O–H bending bands observed in the FTIR spectra.

The Si 2p spectrum (Fig. 4d) exhibits a characteristic peak centred at approximately 101.7 eV, corresponding to Si^{4+} in Si–O–Si and Si–O–Al environments of the aluminosilicate framework. Similarly, the Al 2p spectrum (Fig. 4e) displays a peak at approximately 74.4 eV, assigned to tetrahedrally coordinated Al^{3+} in the zeolite structure [45]. The absence of additional silicon- or aluminium-containing species indicates that the zeolite framework remains chemically stable during the solution-assisted composite preparation. The C 1s spectrum (Fig. 4f) consists of a dominant peak at 284.8 eV attributed to adventitious C–C/C–H species together with a weak component near 286.3 eV corresponding to C–O functionalities. These carbon species arise from unavoidable atmospheric contamination and serve only as the reference for charge calibration. Overall, the XPS results provide clear evidence for the coexistence of Zn^{2+}, Ti^{4+}, Si^{4+}, Al^{3+}, lattice oxygen, and framework sodium in the ZT-40 composite. The oxidation states of the constituent elements remain unchanged after composite formation, indicating that the solution-assisted mixing process preserves the chemical identities of both $ZnTiO_3$ and the zeolite framework. These observations are in good agreement with the PXRD results, which confirm the coexistence of crystalline $ZnTiO_3$, Zn_2TiO_4, and zeolite phases, and with the FTIR spectra, which retain the characteristic metal–oxygen and aluminosilicate framework vibrations. Collectively, these complementary characterisation techniques demonstrate the successful fabrication of a chemically stable $ZnTiO_3$/zeolite composite with intimate interfacial contact between the oxide and porous aluminosilicate phases, providing a suitable structural framework for subsequent electrochemical investigations.

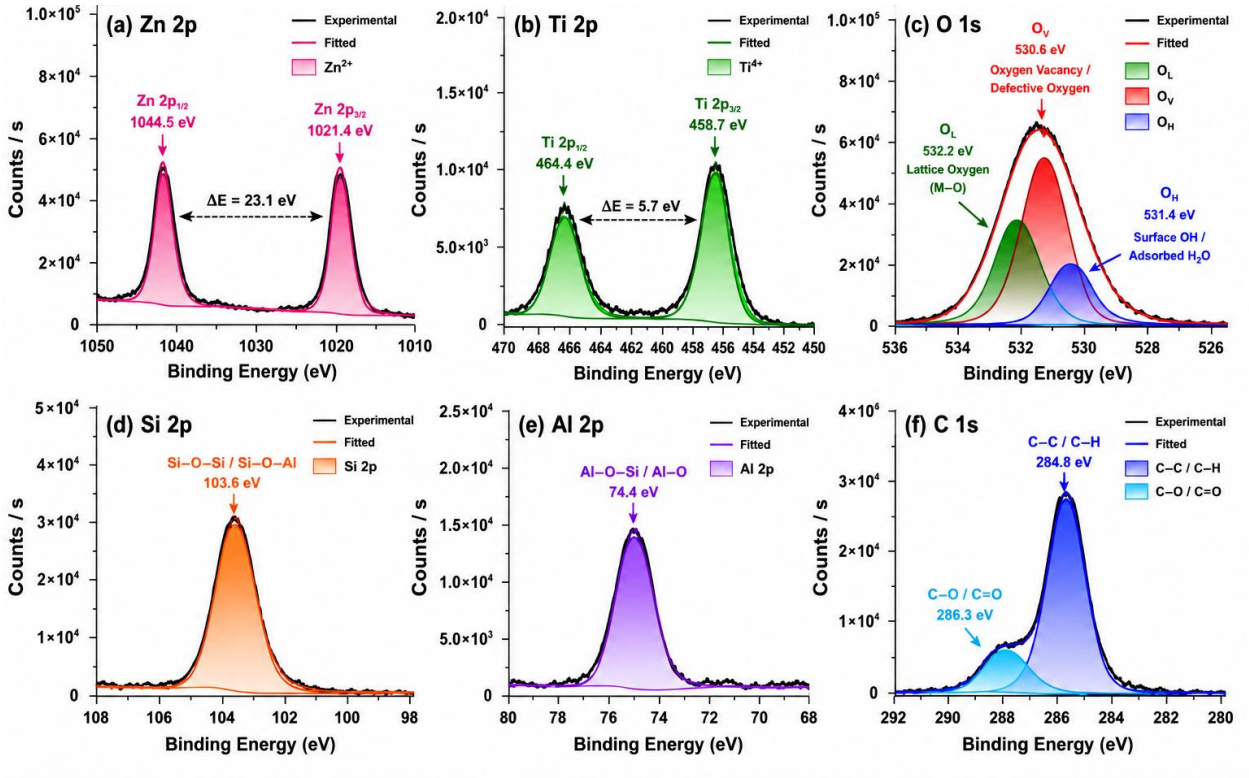


Fig. 4. Deconvoluted high-resolution XPS spectra of the ZT-40 sample showing the Zn 2p, Ti 2p, O 1s, Si 2p, Al 2p, and C 1s core levels.

Table 1. Surface elemental concentrations of the ZT-40 composite derived from XPS survey spectra.

Element	Core Level	Binding Energy (eV)	Atomic Composition (at.%)
O	O 1s	530.93, 530.67	41.42
C*	C 1s	284.37	31.67
Al	Al 2p	73.84, 73.44	8.15
Si	Si 2p	101.73, 101.29	7.80
Na	Na 1s	1071.78	5.29
Zn	Zn 2p	1021.25, 1021.05	3.08
Ti	Ti 2p	457.90, 457.45	2.58

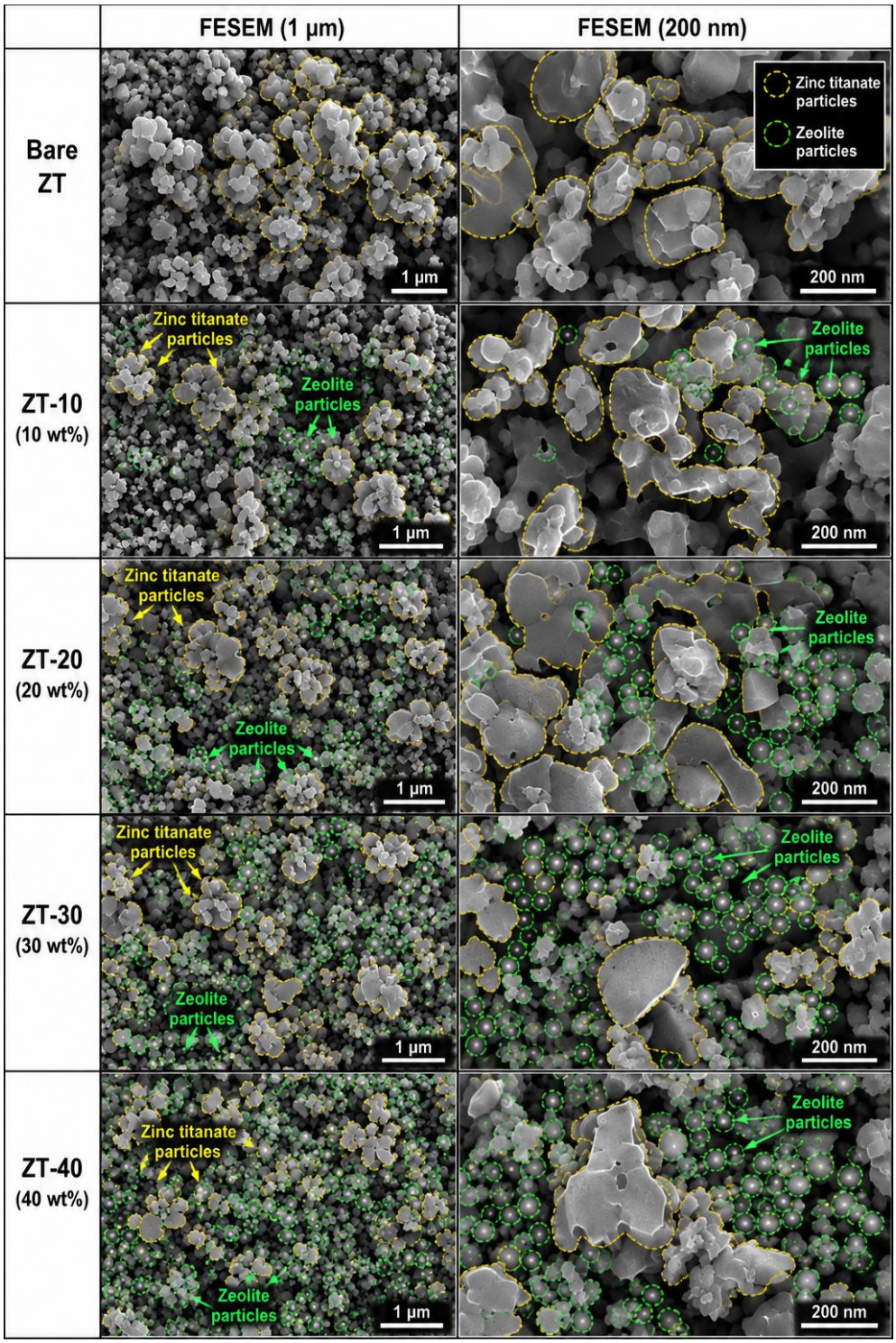
**Adventitious carbon used for charge correction.*

3.4. FESEM Surface Morphology Analysis

The surface morphology of pristine $ZnTiO_3$ (ZT) and $ZnTiO_3$/zeolite composites with different zeolite loadings was investigated by field-emission scanning electron microscopy (FESEM), and the corresponding micrographs are presented in Fig. 5. The images reveal a gradual evolution in the microstructure with increasing zeolite content while preserving the overall morphology of the zinc titanate phase. The pristine ZT sample consists of irregularly shaped particles that are strongly agglomerated, forming dense clusters with relatively smooth surfaces. Such agglomeration is commonly observed for zinc titanate synthesised by high-temperature solid-state reactions, where particle coalescence and partial sintering occur during calcination at elevated temperatures.

Following the incorporation of 10 wt% zeolite (ZT-10), finer particles become distributed around the larger $ZnTiO_3$ aggregates. These particles occupy the interparticle regions without noticeably altering the morphology of the zinc titanate grains, indicating good physical integration between the two components. Increasing the zeolite content to 20 wt% (ZT-20) results in a more homogeneous distribution of the secondary phase throughout the composite. The interparticle voids are progressively filled, resulting in a more interconnected microstructure with reduced direct contact between adjacent zinc titanate aggregates. Further increasing the zeolite loading to 30 wt% (ZT-30) yields a more uniform composite morphology, with zinc titanate particles surrounded by the porous aluminosilicate phase. The dispersion of the secondary phase becomes more continuous, reducing the extent of large agglomerates observed in the pristine sample. No evidence of particle cracking or phase segregation is observed, suggesting good compatibility between the oxide and zeolite components during the solution-assisted mixing process.

Among the investigated compositions, the ZT-40 composite exhibits the most homogeneous microstructure. The FESEM images show that the zinc titanate particles remain well preserved while being uniformly distributed within the porous zeolite matrix. The composite displays a comparatively open and interconnected morphology with numerous interparticle voids that are characteristic of the incorporated zeolite. The absence of large isolated agglomerates indicates that the zeolite phase is effectively dispersed throughout the composite. The morphological observations are consistent with the PXRD results, which confirm the coexistence of crystalline $ZnTiO_3$ and zeolite without the formation of additional crystalline phases, and with the XPS analysis, which verifies the presence of Zn, Ti, Si, Al, and O on the composite surface. Collectively, these results demonstrate that the solution-assisted synthesis route produces a structurally homogeneous $ZnTiO_3$/zeolite composite while preserving the individual characteristics of both constituent phases. The gradual reduction in particle agglomeration together with the formation of a more open composite structure is expected to improve electrolyte accessibility, which is advantageous for subsequent electrochemical charge-storage applications.



394

395 **Fig. 5.** FESEM images of pristine $ZnTiO_3$ (ZT) and zinc titanate/zeolite composites (ZT-
396 10, ZT-20, ZT-30, and ZT-40) with increasing zeolite content, recorded at 1 μm and 200 nm
397 scales. The micrographs illustrate the morphological evolution and progressive distribution of
398 zeolite particles within the zinc titanate matrix.
399

3.5. Particle-Size Distribution Analysis

The particle-size distributions of pristine $ZnTiO_3$ and the $ZnTiO_3$/zeolite composites were determined from FESEM micrographs by measuring more than 150 particles for each sample using ImageJ software, followed by Gaussian fitting of the experimental data (Fig. S2). The histograms exhibit unimodal distributions with satisfactory Gaussian fits, indicating a relatively uniform particle population across all compositions. The pristine $ZnTiO_3$ sample exhibits an average particle size of 103.3 ± 34.6 nm (n = 156). Upon incorporation of zeolite, the average particle size increases progressively to 142.7 ± 46.1 nm (ZT-10), 168.9 ± 54.5 nm (ZT-20), 227.6 ± 70.8 nm (ZT-30), and 251.3 ± 74.9 nm (ZT-40). Simultaneously, the particle-size distributions broaden with increasing zeolite content, indicating the formation of composite particles with a wider size range. The gradual increase in the measured particle size is attributed to the physical assembly of $ZnTiO_3$ particles with the porous zeolite phase rather than intrinsic grain growth of the zinc titanate crystallites. As observed in the FESEM images, zeolite particles occupy the interparticle regions and progressively surround the $ZnTiO_3$ aggregates, resulting in larger composite assemblies. This interpretation is supported by the PXRD results, which show no evidence of significant crystal growth or phase transformation following zeolite incorporation.

Although the average composite particle size increases, FESEM observations show that the microstructure becomes less densely agglomerated and more open as zeolite loading increases. Consequently, the measured particle size represents the overall dimensions of the $ZnTiO_3$/zeolite composite particles rather than the crystallite size of the zinc titanate phase. Among the investigated samples, ZT-40 exhibits the largest average particle size together with the most homogeneous dispersion of the zeolite phase, indicating effective integration of the two components. The combined particle-size and FESEM analyses therefore confirm that the solution-assisted mixing process produces well-dispersed $ZnTiO_3$/zeolite composite particles while preserving the crystalline structure of the zinc titanate phase.

3.6. Energy-Dispersive X-ray Spectroscopy (EDS) Analysis

The elemental composition and spatial distribution of the ZT-40 composite were investigated by energy-dispersive X-ray spectroscopy (EDS), and the corresponding spectrum together with elemental mapping images are presented in Fig. 6. The EDS spectrum confirms the presence of

Zn, Ti, O, Si, Al, and Na, corresponding to the constituent elements of the $ZnTiO_3$ and zeolite phases. No additional elemental peaks associated with undesirable impurities are detected, indicating the high chemical purity of the composite. The quantitative elemental composition obtained from EDS is summarised in the Tables in the respective Figs. 6 and S3-S6. Oxygen constitutes the major element, consistent with the oxide and aluminosilicate frameworks of the composite. The simultaneous presence of Zn and Ti verifies the zinc titanate phase, whereas Si, Al, and Na confirm the successful incorporation of the zeolite framework. The measured elemental ratios agree well with the nominal composition of the composite and are consistent with the phase assemblage identified by PXRD.

Elemental mapping demonstrates that Zn, Ti, O, Si, Al, and Na are uniformly distributed throughout the analysed region. The Zn and Ti signals overlap across the particles, confirming the homogeneous distribution of the zinc titanate phase, while the Si, Al, and Na signals are evenly dispersed, indicating effective incorporation of the zeolite component without detectable phase segregation or localised enrichment. The oxygen map exhibits a continuous distribution over the entire composite, reflecting the oxide and aluminosilicate frameworks. The EDS observations complement the XPS analysis, which identifies the corresponding surface chemical states of Zn^{2+}, Ti^{4+}, Si^{4+}, Al^{3+}, and lattice oxygen, and are consistent with the PXRD results confirming the coexistence of crystalline $ZnTiO_3$, Zn_2TiO_4, and zeolite phases. Together, these results demonstrate that the solution-assisted synthesis route produces a chemically homogeneous $ZnTiO_3$/zeolite composite with uniform elemental distribution and without detectable impurity phases.

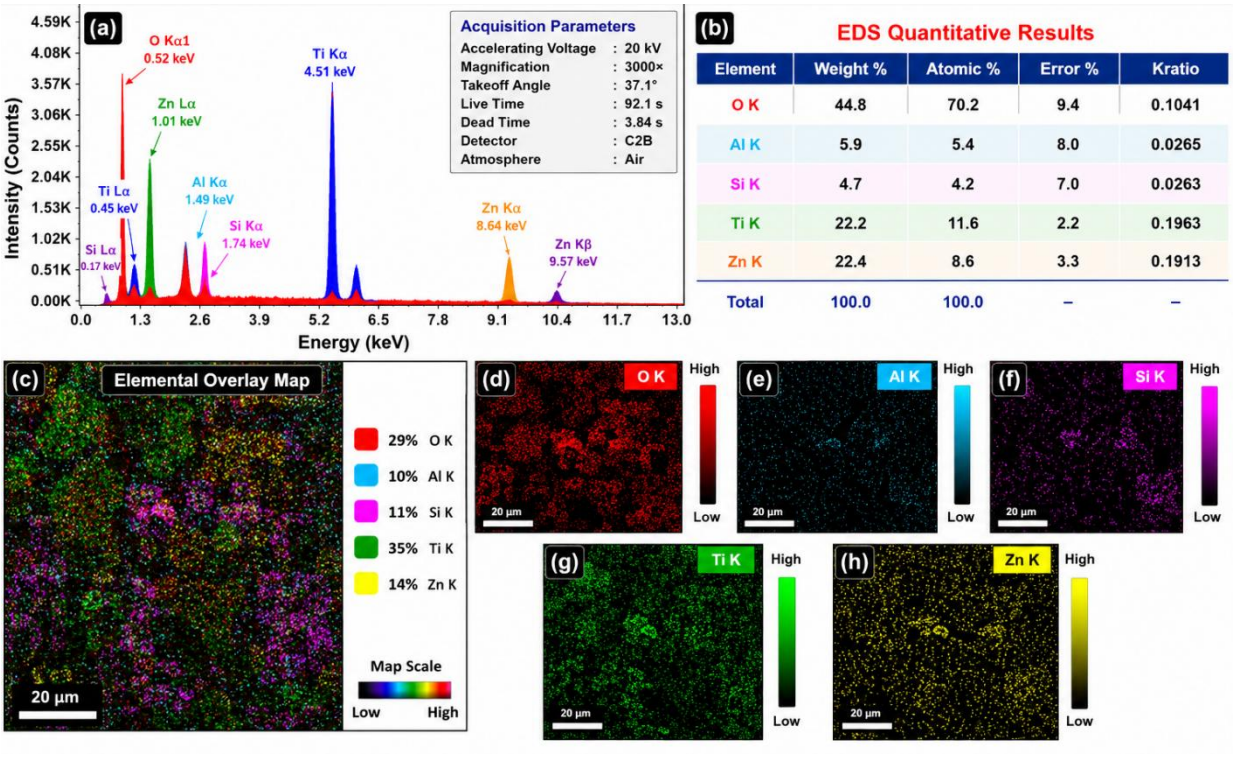


Fig.6. EDS characterization of the ZT-40 composite: (a) EDS spectrum with characteristic X-ray peak assignments, (b) quantitative elemental composition, (c) elemental overlay map, and corresponding elemental distribution maps of (d) O, (e) Al, (f) Si, (g) Ti, and (h) Zn, confirming the homogeneous distribution of the constituent elements throughout the $ZnTiO_3$/zeolite composite.

3.7 Electrochemical Performance: Cyclic Voltammetry Analysis

The electrochemical charge-storage behaviour of pristine $ZnTiO_3$ (ZT) and $ZnTiO_3$/zeolite composite electrodes was investigated by cyclic voltammetry (CV) using a three-electrode configuration in 3 M KOH aqueous electrolyte over scan rates ranging from 1 to 100 mV s^{-1} (Fig. 7). All electrodes exhibit well-defined anodic and cathodic redox peaks rather than nearly rectangular electric double-layer capacitor (EDLC) profiles, confirming that charge storage is predominantly governed by reversible Faradaic redox reactions of the $ZnTiO_3$ phase. The retention of distinct redox peaks over the entire scan-rate range demonstrates good electrochemical reversibility and structural stability during repeated OH^- ion insertion and extraction [28,29,46]. As the scan rate increases from 1 to 100 mV s^{-1}, the anodic and cathodic peak currents increase progressively, accompanied by a gradual increase in the enclosed CV area for all electrodes. Simultaneously, the oxidation and reduction peaks shift slightly towards more positive and negative potentials, respectively, owing to electrode polarisation and diffusion

limitations at higher scan rates. These shifts arise because electrolyte ions require additional overpotential to access electrochemically active sites when the scan rate increases. Nevertheless, the CV profiles retain their characteristic shape without significant distortion, indicating rapid electron-transfer kinetics and good rate capability for all $ZnTiO_3$/zeolite composite electrodes.

The incorporation of zeolite markedly influences the electrochemical response of $ZnTiO_3$ by enhancing electrolyte accessibility and improving ion-transport pathways. Compared with pristine ZT, all composite electrodes exhibit higher current responses and larger integrated CV areas, confirming that the porous aluminosilicate framework enhances charge storage. Among the investigated compositions, ZT-20 and ZT-40 exhibit the most pronounced electrochemical responses, with substantially larger CV areas than those of pristine ZT, ZT-10, and ZT-30. The enhanced performance is attributed to the synergistic interaction between the pseudocapacitive $ZnTiO_3$ phase and the hierarchical porous structure of zeolite, which promotes rapid electrolyte penetration, increases the electrochemically accessible surface area, and suppresses particle agglomeration.

Although ZT-40 exhibits a comparatively high current response due to its higher zeolite content and improved electrolyte accessibility, the ZT-20 electrode provides the most balanced electrochemical behaviour, with intense, well-defined redox peaks and the largest effective charge-storage capability. This indicates that an optimal zeolite loading exists, in which the porous framework sufficiently enhances ion transport while maintaining a high concentration of electrochemically active $ZnTiO_3$. At higher zeolite loading (ZT-40), the increased proportion of the electrochemically inactive aluminosilicate phase can partially dilute the redox-active $ZnTiO_3$, thereby limiting further improvement in overall charge-storage performance despite the larger accessible surface area. The electrochemical behaviour is in good agreement with the structural and morphological characterisation results. PXRD confirms that the crystalline $ZnTiO_3$ and Zn_2TiO_4 phases remain unchanged after composite formation, while FESEM reveals improved particle dispersion and a more open porous architecture following zeolite incorporation. XPS further demonstrates the preservation of the Zn^{2+} and Ti^{4+} oxidation states, as well as intimate interfacial contact between the zinc titanate and aluminosilicate phases. Collectively, these observations indicate that the enhanced electrochemical performance originates from the optimised composite architecture rather than changes in the intrinsic crystal or electronic

structure of $ZnTiO_3$. The superior overall electrochemical performance of ZT-20, subsequently confirmed by the GCD, EIS, and cycling stability analyses, demonstrates that 20 wt% zeolite provides the optimum balance between electrolyte transport, active-site accessibility, and the retention of redox-active $ZnTiO_3$, whereas ZT-40 primarily benefits from enhanced porosity but contains a comparatively higher fraction of electrochemically inactive zeolite.

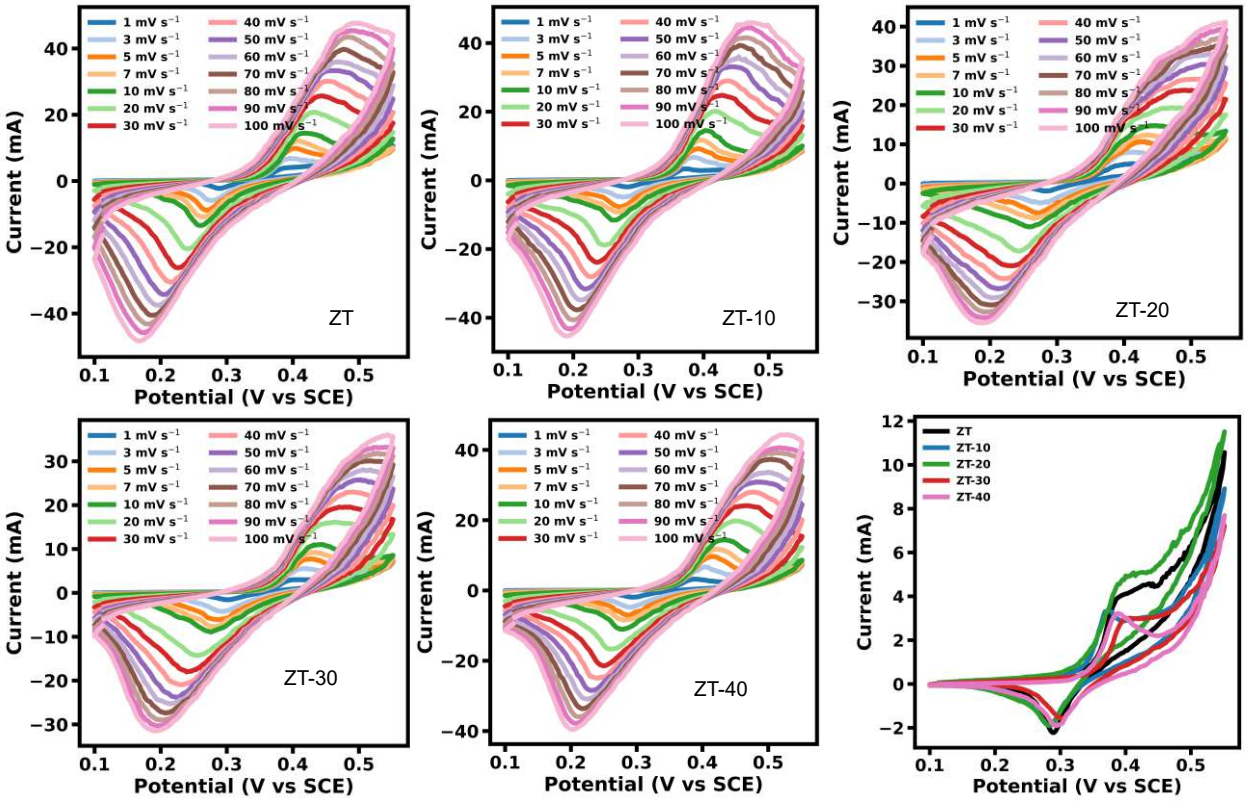


Fig. 7. Cyclic voltammetry (CV) curves of pristine $ZnTiO_3$ (ZT) and $ZnTiO_3$/zeolite composite electrodes (ZT-10, ZT-20, ZT-30, and ZT-40) recorded in 3 M KOH using a three-electrode configuration at scan rates ranging from 1 to 100 mV s^{-1}.

3.8. Charge-storage kinetics analysis using the power-law relationship

To elucidate the charge-storage kinetics of the $ZnTiO_3$/zeolite electrodes, the dependence of peak current (i) on scan rate (v) was analysed using the power-law relationship ($i = av^b$). The corresponding log(i)–log(v) plots for the anodic and cathodic peaks are presented in Fig. 8(a–e), and the calculated anodic and cathodic b-values are summarised in Table 2. According to the power-law model, a b value of approximately 0.5 indicates a diffusion-controlled Faradaic

process, whereas $b \approx 1$ corresponds to an ideal surface-controlled capacitive process. Intermediate values indicate the coexistence of both charge-storage mechanisms.

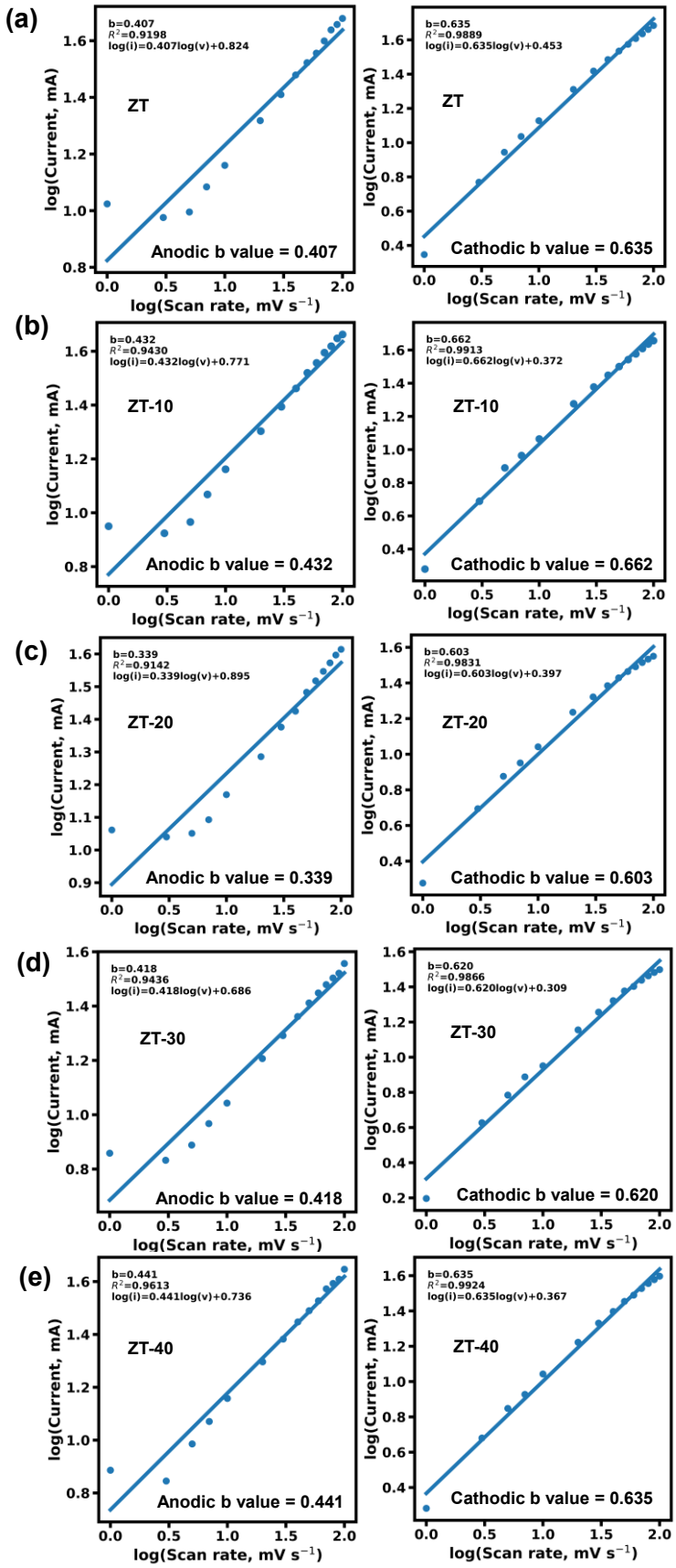
The anodic *b*-values of the ZT, ZT-10, ZT-20, ZT-30, and ZT-40 electrodes were determined to be 0.407, 0.432, 0.339, 0.418, and 0.441, respectively, whereas the corresponding cathodic *b*-values were 0.635, 0.662, 0.603, 0.620, and 0.635. The anodic *b*-values, being closer to 0.5 than to 1.0, indicate that the oxidation process is predominantly governed by diffusion-controlled Faradaic reactions. In contrast, the higher cathodic *b*-values (0.603–0.662) suggest that the reduction process involves mixed charge-storage behaviour arising from the combined contributions of diffusion-controlled ion insertion and surface-controlled pseudocapacitive reactions.

Among the investigated electrodes, ZT-40 exhibits the highest anodic *b*-value (0.441), while ZT-10 shows a comparable value (0.432), indicating a relatively greater surface-controlled contribution during oxidation. Although ZT-20 exhibits the lowest anodic *b*-value (0.339), it demonstrates the best overall electrochemical performance in the subsequent GCD and EIS analyses, indicating that the overall charge-storage capability is governed not only by the kinetic parameter (*b*) but also by factors such as charge-transfer resistance, electrolyte accessibility, ion-diffusion pathways, and active material utilisation. The incorporation of zeolite improves electrolyte penetration and increases the electrochemically active interfacial area, while the optimum 20 wt% zeolite loading provides the most favourable balance between rapid ion transport and the retention of sufficient redox-active $ZnTiO_3$. It should be noted that the power-law analysis provides only a qualitative assessment of the dominant charge-storage mechanism based on peak-current behaviour. The *b*-value alone cannot quantify the individual contributions of surface-controlled and diffusion-controlled processes over the entire potential window. Therefore, a more rigorous quantitative evaluation was subsequently carried out using Dunn's method, which separates the measured current into capacitive and diffusion-controlled components and enables direct determination of their respective contributions to the overall charge-storage behaviour.

Table 2. Electrochemical kinetic parameters obtained from the power-law analysis of pristine $ZnTiO_3$ (ZT) and $ZnTiO_3$/zeolite composite electrodes. The anodic and cathodic b-values were determined from the linear relationship between log(i) and log(v) according to the equation $i = av^b$.

Sample	Anodic *b* value	R^2	Cathodic *b* value	R^2	Interpretation of charge-storage kinetics*
ZT	0.407	0.9198	0.635	0.9889	Diffusion-controlled anodic process; mixed diffusion- and surface-controlled cathodic process
ZT-10	0.432	0.9430	0.662	0.9913	Predominantly diffusion-controlled anodic process with relatively greater surface-controlled contribution during reduction
ZT-20	0.339	0.9142	0.603	0.9831	Strongly diffusion-controlled anodic process; mixed cathodic kinetics
ZT-30	0.418	0.9436	0.620	0.9866	Diffusion-controlled anodic process with mixed cathodic charge storage
ZT-40	0.441	0.9613	0.635	0.9924	Diffusion-dominated charge storage with an enhanced surface-controlled contribution

**The kinetic interpretation presented in this table is qualitative and based solely on the power-law (b-value) analysis. The relative contributions of diffusion-controlled and surface-controlled charge storage cannot be quantified using the b-value alone and are evaluated in the subsequent section using Dunn's method.*


(a)
b=0.407
R^2=0.9198
log(i)=0.407log(v)+0.824
ZT
Anodic b value = 0.407
b=0.635
R^2=0.9889
log(i)=0.635log(v)+0.453
ZT
Cathodic b value = 0.635
(b)
b=0.432
R^2=0.9430
log(i)=0.432log(v)+0.771
ZT-10
Anodic b value = 0.432
b=0.662
R^2=0.9913
log(i)=0.662log(v)+0.372
ZT-10
Cathodic b value = 0.662
(c)
b=0.339
R^2=0.9142
log(i)=0.339log(v)+0.895
ZT-20
Anodic b value = 0.339
b=0.603
R^2=0.9831
log(i)=0.603log(v)+0.397
ZT-20
Cathodic b value = 0.603
(d)
b=0.418
R^2=0.9436
log(i)=0.418log(v)+0.686
ZT-30
Anodic b value = 0.418
b=0.620
R^2=0.9866
log(i)=0.620log(v)+0.309
ZT-30
Cathodic b value = 0.620
(e)
b=0.441
R^2=0.9613
log(i)=0.441log(v)+0.736
ZT-40
Anodic b value = 0.441
b=0.635
R^2=0.9924
log(i)=0.635log(v)+0.367
ZT-40
Cathodic b value = 0.635
log(Current, mA)
log(Scan rate, mV s^{-1})

557

Fig. 8. Determination of the charge-storage kinetics of pristine $ZnTiO_3$ (ZT) and $ZnTiO_3$/zeolite composite electrodes (ZT-10, ZT-20, ZT-30, and ZT-40) from the relationship between peak current and scan rate. Linear fittings of log(i) versus log(v) for the anodic and cathodic peaks were used to determine the b-values**.**

3.9 Dunn's Kinetic Analysis

To quantitatively evaluate the charge-storage mechanism of the $ZnTiO_3$/zeolite electrodes, Dunn's method was employed by separating the measured current into surface-controlled and diffusion-controlled components according to:

$$i(V) = k_1 v + k_2 v^{1/2} \qquad (6)$$

where $k_1 v$ represents the surface-controlled current and $k_2 v^{1/2}$ corresponds to the diffusion-controlled Faradaic current. Unlike the power-law (*b*-value) analysis, which provides only qualitative information regarding the dominant charge-storage mechanism, Dunn's method enables quantitative separation of the current contributions over the entire potential window and is therefore regarded as a more rigorous approach for evaluating electrochemical kinetics.

The reconstructed currents exhibited good agreement with the experimental cyclic voltammograms, demonstrating that the Dunn model adequately describes the electrochemical behaviour of the investigated electrodes. For the pristine $ZnTiO_3$ electrode (listed in Table S1), the reconstructed current yielded an RMSE of 0.0030 and an MAE of 0.0018 at 100 mV s^{-1}, while the ZT-20 composite exhibited comparable reconstruction errors (RMSE = 0.0032 and MAE = 0.0019), confirming satisfactory agreement between the reconstructed and experimental currents. The relatively small reconstruction errors indicate that the calculated k_1 and k_2 coefficients adequately capture the dominant electrochemical processes.

The quantitative current separation reveals that diffusion-controlled Faradaic reactions dominate the charge-storage behaviour of both electrodes. The quantitative variation of the capacitive and diffusion-controlled contributions as a function of scan rate is illustrated in Fig. 9 and the

583 respective values are listed in Table S2 , providing further insight into the charge-storage kinetics
584 of the ZT and ZT-20 electrodes. For the pristine ZT electrode, the diffusion-controlled
585 contribution accounted for approximately 71.07% of the total current at 100 mV s^{-1}, whereas the
586 capacitive contribution was 28.93%. Upon incorporation of 20 wt% zeolite, the surface-
587 controlled contribution increased to 35.98%, accompanied by a corresponding decrease in the
588 diffusion-controlled contribution to 64.02%. The increased capacitive contribution demonstrates
589 that the porous zeolite framework enhances electrolyte accessibility, increases the
590 electrochemically active surface area, and promotes faster interfacial charge-transfer reactions
591 while maintaining diffusion-dominated charge storage.
592 The enhanced surface-controlled contribution observed for the ZT-20 composite can be directly
593 correlated with the structural characteristics identified by the FESEM and XPS analyses. The
594 homogeneous dispersion of $ZnTiO_3$ particles within the porous aluminosilicate matrix provides
595 additional electrolyte–electrode interfaces, suppresses particle agglomeration, and shortens OH^-
596 diffusion pathways, thereby facilitating rapid charge transfer while preserving the intrinsic
597 battery-type Faradaic behaviour of $ZnTiO_3$. Although the quantitative Dunn analysis was
598 performed for the pristine ZT and the optimized ZT-20 electrode, the improved electrochemical
599 response observed for the ZT-40 electrode in the cyclic voltammetry studies likewise suggests
600 that the higher zeolite content enhances electrolyte accessibility and interfacial charge transfer.
601 However, the superior overall electrochemical performance of ZT-20, as confirmed by the GCD,
602 EIS, and cycling stability analyses, indicates that 20 wt% zeolite provides the optimum balance
603 between surface-controlled kinetics and the availability of electrochemically active $ZnTiO_3$,
604 whereas further increasing the zeolite content primarily improves porosity but also increases the
605 fraction of electrochemically inactive aluminosilicate. Overall, the Dunn analysis confirms that

pristine $ZnTiO_3$ and $ZnTiO_3$/zeolite composites exhibit mixed charge-storage kinetics dominated by diffusion-controlled Faradaic reactions, with zeolite incorporation increasing the contribution of rapid, surface-controlled processes. These quantitative findings are consistent with the qualitative interpretation obtained from the power-law (*b*-value) analysis and further demonstrate that the porous zeolite framework enhances electrolyte transport and active-site utilisation without altering the intrinsic battery-type charge-storage mechanism of $ZnTiO_3$.

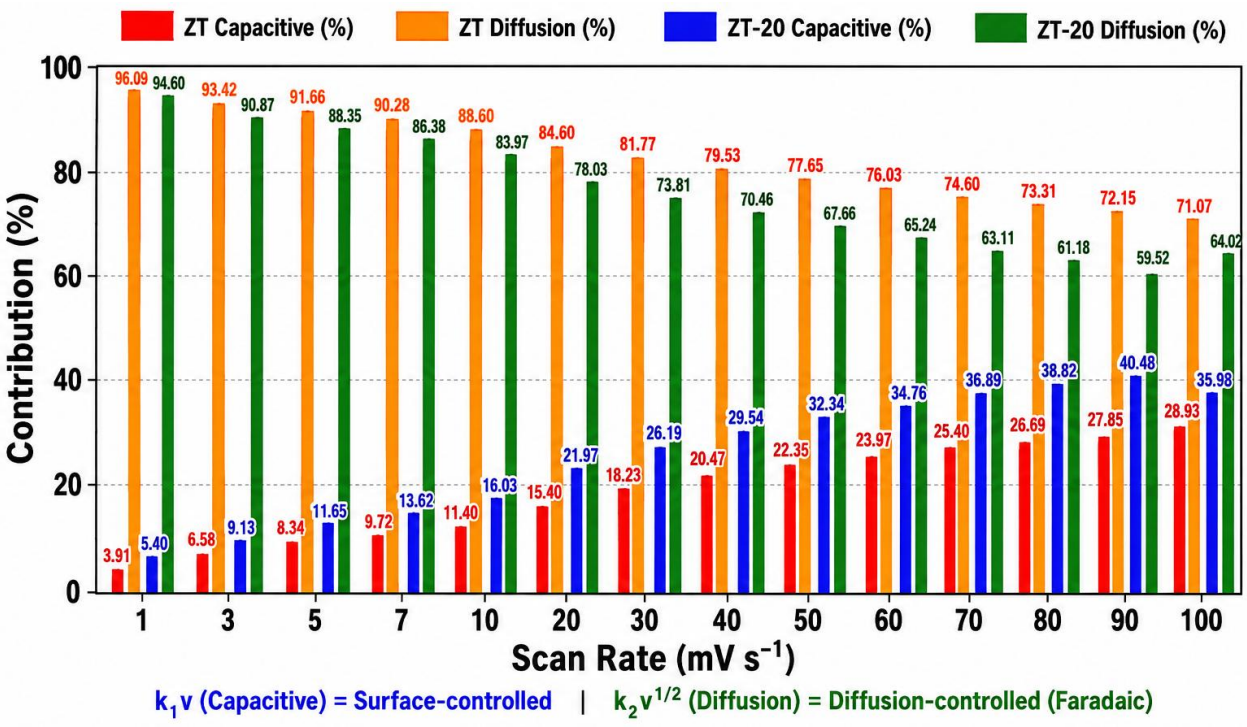


Fig. 9. Quantitative separation of surface-controlled (capacitive) and diffusion-controlled current contributions of the ZT and ZT-20 electrodes determined by Dunn's kinetic analysis.

3.10 Galvanostatic Charge–Discharge Performance

The charge-storage characteristics of the pristine $ZnTiO_3$ (ZT) and $ZnTiO_3$/zeolite composite electrodes were further evaluated by galvanostatic charge–discharge (GCD) measurements in 3 M KOH over a current density range of 1–5 A g^{-1}, and the corresponding curves are presented in Fig. 10. All electrodes exhibit nearly symmetric charge–discharge profiles with distinct potential

plateaus, indicating that the electrochemical response is predominantly governed by reversible Faradaic redox reactions rather than ideal electric double-layer capacitance. The slight deviation from linearity observed during both charging and discharging further confirms the battery-type charge-storage behaviour of the $ZnTiO_3$-based electrodes. As expected, the discharge time decreased progressively with increasing current density for all electrodes because the shorter charging/discharging duration at higher current densities limits electrolyte ion diffusion and reduces the utilisation of electrochemically active sites. Nevertheless, all electrodes retained their characteristic discharge profiles across the investigated current-density range, demonstrating good electrochemical reversibility and stable charge-transfer kinetics.

A comparison of the GCD curves recorded at 1 A g^{-1} (Fig.10) reveals a clear influence of zeolite incorporation on the electrochemical performance. Among the investigated electrodes, ZT-20 exhibits the longest discharge time (149.0 s), corresponding to the highest specific capacity of 149.0 C g^{-1} (41.39 mAh g^{-1}), whereas the pristine ZT electrode delivers 134.0 C g^{-1} (37.22 mAh g^{-1}) (Table 3). The approximately 11.2% enhancement relative to pristine $ZnTiO_3$ indicates that incorporating 20 wt% zeolite effectively improves charge-storage performance. This improvement can be attributed to the porous aluminosilicate framework of the zeolite, which increases electrolyte accessibility, facilitates OH^- ion transport, shortens diffusion pathways, and exposes more electrochemically active $ZnTiO_3$ sites for Faradaic reactions.

Further increasing the zeolite content beyond the optimum level led to a gradual decline in electrochemical performance. The ZT-30 and ZT-40 electrodes delivered specific capacities of 99.0 C g^{-1} (27.50 mAh g^{-1}) and 112.9 C g^{-1} (31.36 mAh g^{-1}), respectively, both lower than that of the pristine ZT electrode. Similarly, ZT-10 exhibited a capacity of 122.1 C g^{-1} (33.93 mAh g^{-1}), indicating that insufficient zeolite loading does not fully exploit the porous framework's

beneficial effects. The inferior performance observed at both lower and higher zeolite contents suggests that an optimum composition is required to balance the availability of electrochemically active $ZnTiO_3$ with efficient ion transport. Excessive zeolite loading likely dilutes the concentration of redox-active $ZnTiO_3$ and increases the proportion of electrochemically inactive material, thereby reducing the overall Faradaic charge-storage capacity.

The superior electrochemical performance of ZT-20 is consistent with the structural and morphological characterisations as well as the electrochemical kinetic analyses presented in the preceding sections. FESEM observations indicate improved particle dispersion and a more open porous architecture, while the b-value and Dunn's kinetic analyses demonstrate enhanced surface-controlled charge storage without compromising the diffusion-controlled Faradaic mechanism. The combination of efficient electrolyte penetration, improved interfacial charge transfer, and optimised ion diffusion results in enhanced utilisation of the $ZnTiO_3$ active material, thereby producing the highest discharge capacity among all investigated electrodes. Overall, the GCD results demonstrate that incorporating an optimal amount of zeolite significantly improves the electrochemical performance of $ZnTiO_3$ electrodes. Among the investigated compositions, ZT-20 provides the most favourable balance between ion transport and utilisation of electrochemically active material, leading to superior charge-storage capability and confirming its potential as an efficient battery-type electrode material for aqueous alkaline energy-storage applications.

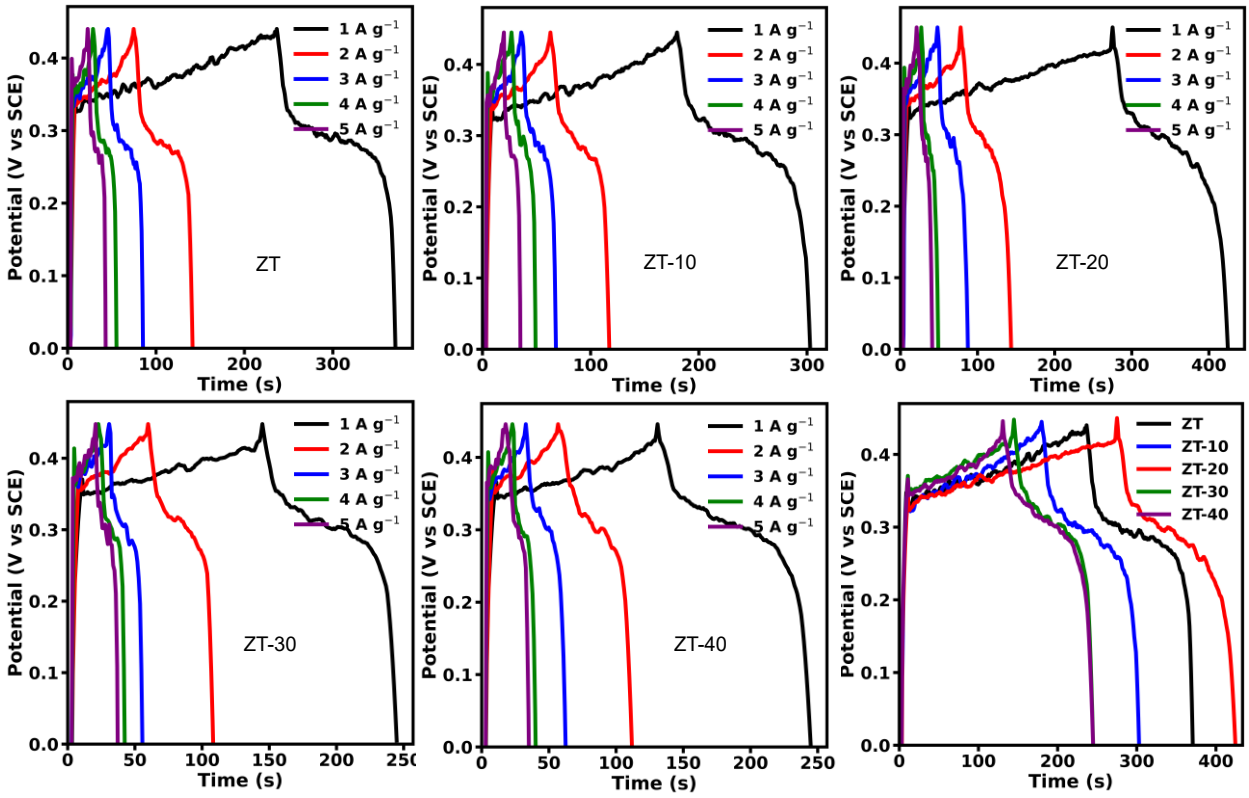


Fig. 10. Galvanostatic charge–discharge (GCD) profiles of $ZnTiO_3$/Zeolite based electrodes measured at different current densities.

Table 3. Electrochemical performance comparison of $ZnTiO_3$-based electrodes at a current density of 1 A g^{-1} in 3 M KOH (three-electrode configuration).

Sample	Discharge Time (s)	Specific Capacity (C g^{-1})	Specific Capacity (mAh g^{-1})
ZT	134.0	134.0	37.22
ZT-10	122.1	122.1	33.93
ZT-20	149.0	149.0	41.39
ZT-30	99.0	99.0	27.50
ZT-40	112.9	112.9	31.36

3.11 Electrochemical Impedance Spectroscopy (EIS)

The electrochemical charge-transfer characteristics of the pristine $ZnTiO_3$ (ZT) and $ZnTiO_3$/zeolite composite electrodes were investigated by electrochemical impedance spectroscopy (EIS), and the corresponding Nyquist plots together with the equivalent electrical circuit are presented in Fig. 11. The spectra consist of a high-frequency intercept, a depressed semicircle in the intermediate-frequency region, and a low-frequency inclined line, representing

the solution resistance (Rs), charge-transfer resistance (Rct), constant phase element (CPE), and Warburg diffusion impedance (W), respectively. The impedance spectra were fitted using the equivalent circuit shown in the inset, and the extracted fitting parameters are summarised in Table 4. The high-frequency intercept corresponding to the electrolyte and intrinsic electrode resistance decreased significantly after zeolite incorporation. The pristine ZT electrode exhibited the highest solution resistance (Rs = 6.82 Ω), whereas the optimized ZT-20 electrode showed the lowest value (Rs = 2.18 Ω). The reduced Rs indicates improved ionic conductivity and enhanced electrode/electrolyte contact resulting from the incorporation of the porous zeolite framework. Although ZT-30 and ZT-40 also exhibited lower Rs than pristine ZT, their values (2.91 Ω and 4.25 Ω, respectively) were higher than that of ZT-20, suggesting that excessive zeolite loading does not further improve electrolyte accessibility. A more pronounced improvement was observed in the charge-transfer resistance. The diameter of the semicircle, representing Rct, decreased from 38.15 Ω for the pristine ZT electrode to only 8.92 Ω for ZT-20, corresponding to a reduction of approximately 76.6%. Such a substantial decrease demonstrates that the optimized zeolite content markedly accelerates the Faradaic charge-transfer process at the electrode/electrolyte interface. In comparison, ZT-10, ZT-30, and ZT-40 exhibited intermediate Rct values of 22.84 Ω, 13.76 Ω, and 27.65 Ω, respectively. These results indicate that although zeolite generally improves charge-transfer kinetics, the maximum enhancement is achieved at 20 wt% loading.

The fitted constant phase element (Q) increased from 0.82×10^{-3} $S \cdot s^n$ for ZT to 2.08×10^{-3} $S \cdot s^n$ for ZT-20, accompanied by an increase in the CPE exponent (n) from 0.81 to 0.89. The higher Q value suggests an increase in the electrochemically accessible interfacial area, while the larger *n* value indicates a surface response closer to ideal capacitive behaviour, reflecting improved

interfacial homogeneity after zeolite incorporation. The decrease in the Warburg coefficient from 47.2 $\Omega\ s^{-1/2}$ for ZT to 18.5 $\Omega\ s^{-1/2}$ for ZT-20 further demonstrates enhanced OH^- ion diffusion within the porous electrode structure. The lower diffusion impedance is consistent with the interconnected pore network provided by the zeolite matrix, which facilitates electrolyte penetration and shortens ion-transport pathways. The quality of the equivalent circuit fitting is confirmed by the low χ^2 values obtained for all electrodes. Among the investigated samples, ZT-20 exhibited the smallest χ^2 value (6.9×10^{-5}), indicating good agreement between the experimental and fitted impedance spectra. This confirms that the selected equivalent circuit adequately describes the electrochemical behaviour of the $ZnTiO_3$/zeolite electrodes.

The EIS results correlate well with the electrochemical measurements discussed in the previous sections. The significantly reduced Rs, Rct, and Warburg impedance, together with the increased interfacial capacitance of the ZT-20 electrode, explain its superior cyclic voltammetry response, highest specific capacity, and enhanced surface-controlled contribution revealed by the Dunn kinetic analysis. The porous zeolite framework improves electrolyte accessibility and facilitates rapid charge transfer while preserving the diffusion-controlled Faradaic charge-storage mechanism of $ZnTiO_3$. Consequently, the optimized ZT-20 composition provides the most efficient charge-transport characteristics among all investigated electrodes, confirming that 20 wt% zeolite represents the optimum loading for enhancing the electrochemical performance of $ZnTiO_3$.

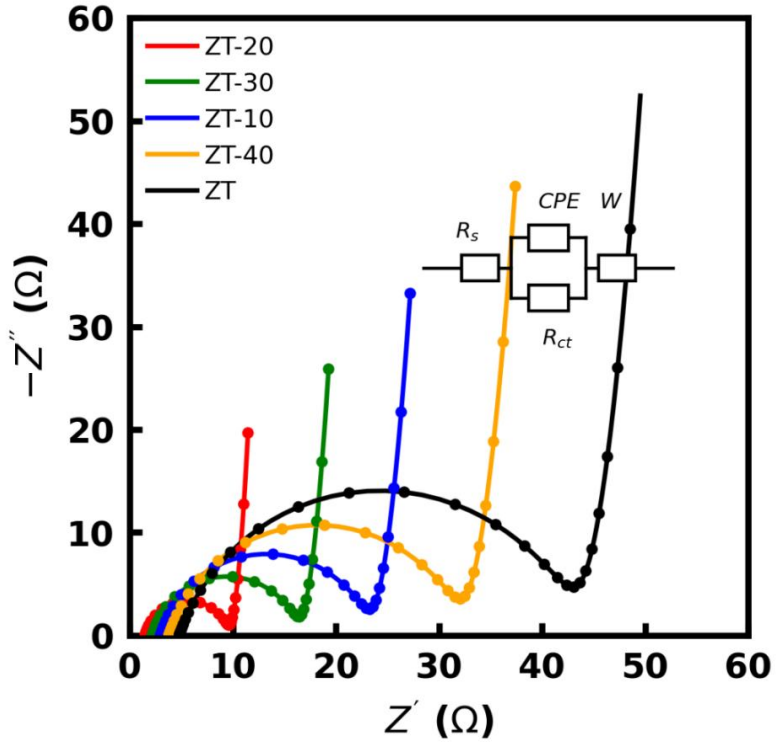


Fig.11. Nyquist plots of the pristine ZT and ZT–zeolite composite electrodes (ZT-10, ZT-20, ZT-30, and ZT-40) recorded in the frequency range of 100 kHz–0.01 Hz, together with the equivalent circuit model Rs–(Rct‖CPE)–W used for impedance fitting.

Table 4. Equivalent circuit fitting parameters of ZT and ZT–zeolite composites obtained using the Rs–(Rct‖CPE)–W model.

Sample	Rs (Ω)	Rct (Ω)	Q (×10^{-3} S·s^{n})	n	σ (Ω s$^{-1/2}$)	χ^2 (×10^{-5})
ZT	6.82	38.15	0.82	0.81	47.2	14.8
ZT-10	3.74	22.84	1.16	0.84	35.4	11.3
ZT-20	2.18	8.92	2.08	0.89	18.5	6.9
ZT-30	2.91	13.76	1.86	0.87	24.7	8.2
ZT-40	4.25	27.65	1.31	0.83	39.8	12.5

3.12 Long-Term Cycling Stability

The long-term electrochemical durability of the optimised ZT-20 electrode was evaluated by continuous galvanostatic charge–discharge (GCD) cycling at a current density of 5 A g^{-1} for

5000 cycles, and the corresponding representative charge–discharge profiles and cycling performance are presented in Fig. 12(a,b). Long-term cycling stability is an essential criterion for practical energy-storage applications because it reflects the electrode's structural integrity and its ability to sustain repeated Faradaic reactions without significant degradation. As shown in Fig. 12(a), the representative GCD curves recorded at the 1st, 1000th, 2000th, 3000th, 4000th, and 5000th cycles retain nearly identical shapes throughout the cycling test. The characteristic battery-type charge–discharge profiles and the corresponding potential plateaus remain well preserved after prolonged cycling, indicating excellent electrochemical reversibility and structural robustness of the ZT-20 electrode. Although a slight reduction in discharge time is observed as the cycle number increases, no noticeable distortion of the charge–discharge profile is observed, suggesting that the electrochemical reaction mechanism remains essentially unchanged during repeated charge–discharge cycles. Furthermore, the relatively small IR drop observed after charging indicates that the electrode maintains low internal resistance even after extended cycling, reflecting stable electrode/electrolyte interfacial contact.

The cycling performance shown in Fig. 12(b) demonstrates a gradual decrease in capacity retention from 100% during the initial cycle to approximately 72% after 5000 cycles. The gradual nature of the capacity decay indicates progressive degradation rather than abrupt structural failure, which is commonly associated with repeated volume changes, partial loss of electrochemically active sites, and increased interfacial resistance during prolonged cycling [36]. Nevertheless, the electrode maintains a substantial fraction of its initial capacity after 5000 cycles, demonstrating satisfactory long-term electrochemical stability for an aqueous battery-type electrode. In addition to capacity retention, the ZT-20 electrode exhibits excellent Coulombic efficiency throughout the cycling test. As illustrated in Fig. 12(b), the Coulombic

efficiency remains nearly constant at approximately 96.3 over the entire 5000-cycle period, indicating highly reversible charge-storage processes with minimal parasitic side reactions. The stable Coulombic efficiency suggests that the $ZnTiO_3$ redox reactions remain highly reversible and that the porous zeolite framework effectively maintains electrolyte accessibility while suppressing irreversible charge loss during repeated cycling.

The favourable cycling stability can be attributed to the synergistic role of the porous zeolite framework within the $ZnTiO_3$ composite. The interconnected aluminosilicate network provides mechanical support, accommodates the stress associated with repeated Faradaic reactions, and facilitates electrolyte penetration and OH^- transport. Consequently, the electrode maintains efficient charge-transfer pathways and preserves a large proportion of its electrochemically active surface throughout prolonged cycling. These observations are consistent with the reduced charge-transfer resistance and enhanced ion diffusion revealed by the EIS analysis, further confirming the beneficial effect of the optimised 20 wt% zeolite incorporation on the long-term electrochemical performance. Overall, the cycling results demonstrate that the ZT-20 electrode combines high specific capacity with good long-term durability and excellent Coulombic efficiency, highlighting its potential as a stable battery-type electrode material for alkaline aqueous energy-storage systems.

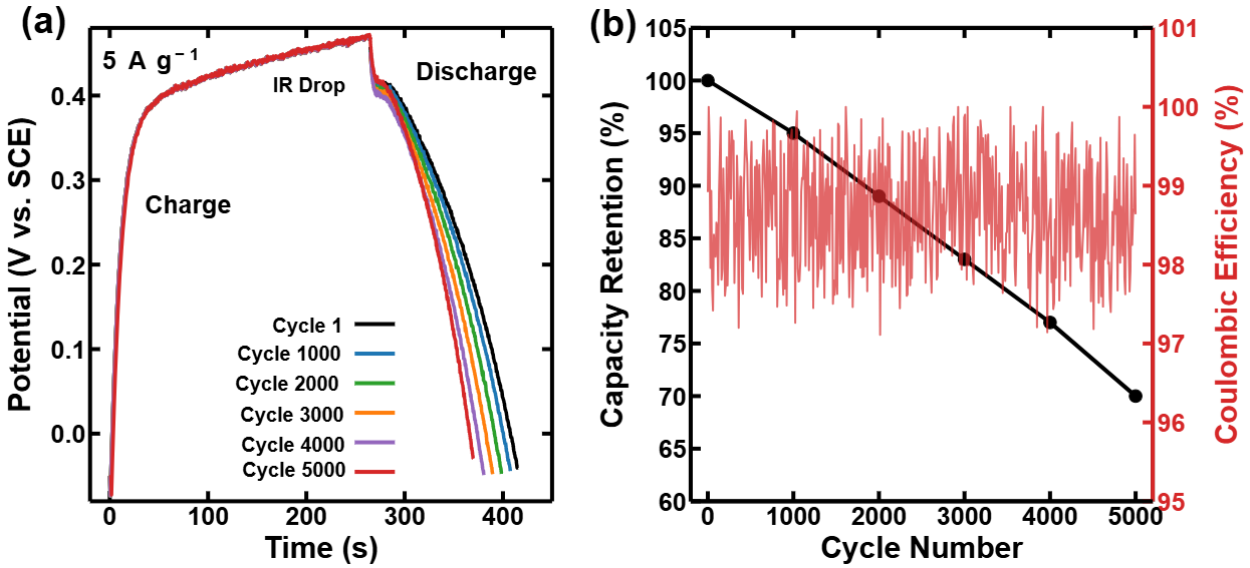


Fig. 12. Long-term cycling performance of the optimized ZT-20 electrode in 3 M KOH at 5 A g^{-1} showing (a) representative GCD curves and (b) capacity retention and Coulombic efficiency over 5000 cycles.

4. Conclusion

$ZnTiO_3$/zeolite composites with different zeolite loadings were successfully synthesised through a simple solution-assisted mixing method and systematically evaluated as supercapattery electrode materials. Structural and surface analyses confirmed the successful integration of crystalline $ZnTiO_3/Zn_2TiO_4$ with the porous zeolite framework while preserving the crystal structure and chemical states of the constituent phases. Zeolite incorporation improved particle dispersion and electrolyte accessibility, thereby enhancing electrochemical kinetics. Electrochemical investigations revealed diffusion-controlled battery-type charge storage with an increased surface-controlled contribution after zeolite incorporation. Among the investigated compositions, ZT-20 exhibited the optimum electrochemical performance, delivering a specific capacity of 149 C g^{-1} (41.39 mAh g^{-1}) at 1 A g^{-1}, a low charge-transfer resistance of 8.92 Ω, and approximately 70% capacity retention after 5000 cycles, demonstrating the importance of balancing porous architecture with the amount of electrochemically active $ZnTiO_3$. Although the present work is limited to a three-electrode evaluation, the results establish $ZnTiO_3$/zeolite composites as promising low-cost electrode materials for alkaline supercapattery applications. Future studies should focus on two-electrode device fabrication, comprehensive porosity

characterisation, and interface engineering to further improve energy-storage performance and practical applicability.

References

1. A. S. Arico, P. Bruce, B. Scrosati, J.-M. Tarascon, and W. Van Schalkwijk, *Nanostructured Materials for Advanced Energy Conversion and Storage Devices* (Nature Publishing Group UK London, 2005), pp. 366–377.
2. P. B.a, L. N, A. Buradi, S. N, P. B l, and V. R, Materials Today: Proceedings **52**, 1309 (2022).
3. S. N. Grigoriev, M. A. Volosova, and A. A. Okunkova, Technologies **12**, 227 (2024).
4. V. K. Verma and S. Verma, Materials Today: Proceedings (2024).
5. R. Kumar, D. Lee, Ü. Ağbulut, S. Kumar, S. Thapa, A. Thakur, R. D. Jilte, C. A. Saleel, and S. Shaik, J Therm Anal Calorim **149**, 1895 (2024).
6. H. Jafarizadeh, E. Yamini, S. M. Zolfaghari, F. Esmaeilion, M. E. H. Assad, and M. Soltani, Energy Reports **12**, 2179 (2024).
7. Z. Zhao, X. Liu, M. Zhang, L. Zhang, C. Zhang, X. Li, and G. Yu, Chem. Soc. Rev. **52**, 6031 (2023).
8. E. T. Sayed, A. G. Olabi, A. H. Alami, A. Radwan, A. Mdallal, A. Rezk, and M. A. Abdelkareem, Energies **16**, 1415 (2023).
9. S. Mohanapriya, S. Alwin, L. Kavitha, and D. Gopi, *Spotlighting the Role of Biopolymer-Derived Green Components for Electrochemical Energy Conversion Devices* (Springer Nature BV, 2025), pp. 3913–3943.
10. N. Singh, S. Khanna, and A. Boora, Sustainable Environmental Engineering 107 (2024).
11. P. Mahajan and M. Sharma, Energy Storage **6**, e634 (2024).
12. A. A. Yadav, Y. M. Hunge, S. Majumder, M. M. Islam, and T. Sakurai, (n.d.).
13. F. Wang, X. Wu, X. Yuan, Z. Liu, Y. Zhang, L. Fu, Y. Zhu, Q. Zhou, Y. Wu, and W. Huang, Chem. Soc. Rev. **46**, 6816 (2017).
14. Y. Wang, L. Zhang, H. Hou, W. Xu, G. Duan, S. He, K. Liu, and S. Jiang, J Mater Sci **56**, 173 (2021).
15. T. Ramachandran, S. S. Sana, K. D. Kumar, Y. A. Kumar, H. H. Hegazy, and S. C. Kim, Journal of Energy Storage **73**, 109096 (2023).
16. A. G. Olabi, Q. Abbas, A. Al Makky, and M. A. Abdelkareem, Energy **248**, 123617 (2022).
17. T. P. Sumangala, M. S. Sreekanth, and A. Rahaman, in *Handbook of Nanocomposite Supercapacitor Materials III*, edited by K. K. Kar (Springer International Publishing, Cham, 2021), pp. 367–393.
18. P. Forouzandeh, V. Kumaravel, and S. C. Pillai, *Electrode Materials for Supercapacitors: A Review of Recent Advances* (MDPI, 2020), p. 969.
19. R. Dubey and V. Guruviah, Ionics **25**, 1419 (2019).
20. P. Gaikwad, N. Tiwari, R. Kamat, S. M. Mane, and S. B. Kulkarni, Materials Science and Engineering: B **307**, 117544 (2024).
21. M. E. Şahin, F. Blaabjerg, and A. Sangwongwanich, (2022).
22. S. Alwin and X. Sahaya Shajan, Mater Renew Sustain Energy **9**, 7 (2020).
23. A. Borenstein, O. Hanna, R. Attias, S. Luski, T. Brousse, and D. Aurbach, *Carbon-Based Composite Materials for Supercapacitor Electrodes: A Review* (The Royal Society of Chemistry, 2017), pp. 12653–12672.

24. J. Lu, D. Li, Y. Chai, L. Li, M. Li, Y. Zhang, and J. Liang, Applied Catalysis B: Environmental **256**, 117800 (2019).
25. P. R. Kumar, S. Alwin, and M. B. Mariyatra, *Perovskite-Structured Ceramic Zinc Titanate Nanomaterials: A Comparative Study of Photovoltaic and Synthetic Approaches* (Elsevier, 2024), pp. 34070–34080.
26. S. Santhiya, P. R. Kumar, S. Alwin, X. S. Shajan, P. S. Renganathan, and J. A. M. Greena, J Inorg Organomet Polym **34**, 501 (2024).
27. M. Sarkar, S. Sarkar, A. Biswas, S. De, P. R. Kumar, E. M. Mothi, and A. Kathiravan, Nano-Structures & Nano-Objects **21**, 100412 (2020).
28. M. Karnan, L. Durai, K. Hari Prakash, and S. Badhulika, Journal of Energy Storage **56**, 106114 (2022).
29. N. K. Sakthivel, M. Govindasamy, and P.-Y. Chen, J. Electrochem. Soc. **172**, 040519 (2025).
30. H. M. Deepa, H. P. Nagaswarupa, R. Naik, N. Basavaraju, J. H. Kim, B. S. Goud, A. N. Alodhayb, and S. Pandiaraj, Appl. Phys. A **131**, 488 (2025).
31. A. B. Abou Hammad, A. M. El Nahrawy, H. S. Magar, and S. Kamel, *Hydroxyethyl Cellulose-Based ZnCe0. 3Ti0. 7O3 Nanocomposites for Sustainable Applications in Supercapacitors and Hydrogen Peroxide Sensors* (The Royal Society of Chemistry, 2026), pp. 1863–1878.
32. S. C. Larsen, J. Phys. Chem. C **111**, 18464 (2007).
33. S. Zallouz, T. Aumond, A. Moissette, A. Sachse, and C. Matei Ghimbeu, ACS Appl. Energy Mater. **7**, 9142 (2024).
34. H. Lu, K. Kim, Y. Kwon, X. Sun, R. Ryoo, and X. S. Zhao, Journal of Materials Chemistry a **6**, 10388 (2018).
35. Y. Gao, J. Wu, W. Zhang, Y. Tan, J. Zhao, and B. Tang, *The Electrochemical Performance of SnO2 Quantum Dots@ Zeolitic Imidazolate Frameworks-8 (ZIF-8) Composite Material for Supercapacitors* (Elsevier, 2014), pp. 208–211.
36. L. Song, Y. Han, F. Guo, Y. Jiao, Y. Li, Y. Liu, and F. Gao, Journal of Nanomaterials **2018**, 1 (2018).
37. S. Ngouana Moafor, L. Macheli, G. L. Kabongo, G. Nyongombe, P. K. Tsobnang, J. N. Lambi, and L. L. Jewell, Microporous and Mesoporous Materials **363**, 112784 (2024).
38. P. Ajay, V. Velkannan, P. Ram Kumar, and M. Kottaisamy, Ceramics International **51**, 751 (2025).
39. N. T. Nolan, M. K. Seery, and S. C. Pillai, (n.d.).
40. L. Budigi, M. R. Nasina, K. Shaik, and S. Amaravadi, ChemInform **46**, (2015).
41. L. BUDIGI, M. R. NASINA, K. SHAIK, and S. AMARAVADI, J Chem Sci **127**, 509 (2015).
42. D. J. Morgan, Surface & Interface Analysis **57**, 28 (2025).
43. A. L. Greenaway, S. Ke, T. Culman, K. R. Talley, J. S. Mangum, K. N. Heinselman, R. S. Kingsbury, R. W. Smaha, M. K. Gish, E. M. Miller, K. A. Persson, J. M. Gregoire, S. R. Bauers, J. B. Neaton, A. C. Tamboli, and A. Zakutayev, Journal American Chemical Society **144**, 13673 (2022).
44. M. Wansleben, J. Vinson, I. Holfelder, Y. Kayser, and B. Beckhoff, X-Ray Spectrometry **48**, 102 (2019).
45. W. J. Malfait and X. Xue, Geochimica et Cosmochimica Acta **74**, 719 (2010).
46. P. Maurya, S. K. Sharma, S. Singh, and S. N. Pandey, Ceramics International **51**, 11541 (2025).

Declaration of Competing Interests

The authors declare no conflicts of interest.

Data availability statement

The manuscript includes all the data used to support the study's findings.

Declaration of generative AI in scientific writing

While preparing this work, the authors used ChatGPT and Grammarly to enhance the writing and language quality. After using these tools, the authors reviewed and edited the content as needed and took full responsibility for the published article.

Author contributions

P. Ram Kumar: Conceptualisation, Methodology, Data Curation, Investigation, Visualisation, Validation, Writing-original draft, Writing and editing. **A. Nichelson:** Investigation, Software, Validation, Data Curation, Writing and editing; **E. Mothi Paul:** Investigation, Validation, Writing and editing. **S. Alwin:** Investigation, Validation, Visualisation, Writing-original draft. **S. Karthickprabhu:** Methodology, Data Curation, Investigation. **Tamilarasan:** Methodology, Data Curation, Investigation.

Acknowledgment

PRK gratefully acknowledges the financial support received from Thiagarajar College of Engineering, Madurai, through the Seed Money Research Grant (Sanction No. R&D Seed_Money/2025/7).

Supplementary Files

This is a list of supplementary files associated with this preprint. Click to download.

- si.docx